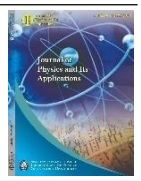
Journal of Physics and Its Applications

Journal homepage : https://ejournal2.undip.ac.id/index.php/jpa/index



# Post-Annealing Structural Evolution of Thermally Evaporated ZnO Thin Films with Emergence of Hydroxide-Related Phases

Isom Hilmi[1*], Muhammad Kevin Adam[1], Bagus Haryadi[1], Valentinus Galih Vidia Putra[2], Niar Gusnaniar[3], Damar Yoga Kusuma[1], Dhias Cahya Hakika[4], and Markus Paramahasti[5]

[1]*Department of Physics, Faculty of Applied Science and Technology, Universitas Ahmad Dahlan, Yogyakarta, Indonesia*
[2]*Basic and Applied Science Research Group, Politeknik STTT Bandung, Bandung, Indonesia*
[3]*Center for Biomedical Research, National Research and Innovation Agency, Bogor, Indonesia*
[4]*Department of Chemical Engineering, Faculty of Industrial Technology, Universitas Ahmad Dahlan, Yogyakarta, Indonesia*
[5]*Department of Physics, Faculty of Mathematics and Natural Sciences, Universitas Gadjah Mada, Yogyakarta, Indonesia*

**Corresponding author: isom.hilmi@fisika.uad.ac.id*

A R T I C L E I N F O

*Article history:*
Received: 06 July 2026
Accepted: 31 August 2026
Available online: 31 August 2026

*Keywords:*
Thin film
ZnO
$Zn(OH)_2$
Annealing
XRD

ABSTRACT

Zinc oxide (ZnO) and zinc hydroxide ($Zn(OH)_2$) are technologically important materials whose structural and optical properties make them attractive for applications in optoelectronics, catalysis, and energy-related devices. In this work, thin films derived from ZnO were fabricated using vacuum thermal evaporation followed by post-deposition annealing at temperatures between 400 and 600 °C. The influence of annealing temperature on the structural, optical, and morphological properties of the films was systematically investigated using X-ray diffraction (XRD), UV–Vis spectroscopy, and scanning electron microscopy (SEM). XRD analysis revealed that the film annealed at 400 °C exhibits a dominant diffraction peak corresponding to the (002) plane of hexagonal wurtzite ZnO, indicating predominant crystallization of the oxide phase. XRD analysis revealed the emergence of diffraction features attributable to hydroxide-containing zinc phases after annealing at 600 °C, accompanied by a substantial reduction in the intensity of characteristic ZnO reflections. Low-energy optical transitions derived from Tauc analysis shifted from approximately 2.75 to 2.00 eV with increasing annealing temperature. These values are interpreted as apparent optical transition energies rather than the intrinsic bandgap of crystalline ZnO or $Zn(OH)_2$. SEM observations further reveal a morphological transition from irregular grains to plate-like and flower-like hierarchical structures that are morphologically consistent with zinc hydroxide-containing systems. The appearance of hydroxide-related phases after high temperature treatment may be associated with post-annealing surface reactions taking place during ambient cooling. However, the underlying mechanism remains to be conclusively established.

## 1. Introduction

Functional metal oxides and hydroxides represent a versatile class of materials that have been widely explored for applications in energy conversion and storage [1, 2], electronics and optoelectronics [3, 4], sensing and actuation [5, 6], photocatalysis and environmental remediation [7-9], photonics [10], and biomedicine [11]. Their technological relevance stems from tuneable electronic structures [12, 13], chemical robustness [14], and compatibility with diverse fabrication routes [15]. Among these materials, zinc-based compounds, particularly zinc oxide (ZnO) and zinc hydroxide ($Zn(OH)_2$), have attracted considerable attention due to their abundance, low cost, and multifunctional physicochemical properties.

ZnO is a well-established wide-bandgap semiconductor whose properties and applications have been extensively documented. Structurally, ZnO can exist in several polymorphic forms, with the hexagonal wurtzite phase (space group $P6_3mc$) being thermodynamically stable under ambient conditions and characterized by lattice parameters $a \approx 0.3296$ nm and $c \approx 0.52065$ nm [16]. A broad range of physical and chemical deposition techniques, including pulsed laser deposition [17], sputtering [18], chemical vapor deposition [19], molecular beam epitaxy [20], and thermal evaporation, have been successfully employed to produce ZnO thin films and nanostructures [21]. Compared with many other deposition approaches, thermal evaporation is characterized by a simple processing scheme, suitability for coating large substrate areas, and good scalability for practical device manufacturing. Moreover, this method enables accurate control of film thickness and promotes uniform film growth. Beyond its intrinsic properties, ZnO is also known to readily undergo chemical and structural modification,

particularly in the presence of moisture or hydroxyl-rich environments.

In contrast to ZnO, zinc hydroxide ($Zn(OH)_2$) has traditionally been regarded as a transient or precursor phase in ZnO synthesis. However, recent studies have demonstrated that $Zn(OH)_2$ can exhibit functional properties in its own right when stabilized in thin-film or nanostructured forms. $Zn(OH)_2$ films have been fabricated via solution-based coating techniques [22], and $ZnO_x/ZnOH_x$ layers prepared by metal–organic decomposition have been shown to function effectively as interlayers in organic photovoltaic devices [22]. Moreover, nanostructured $Zn(OH)_2$, such as nanoflake films synthesized by the successive ionic layer adsorption and reaction (SILAR) method, has been investigated for electrochemical energy storage applications, demonstrating well-defined crystallinity and promising pseudocapacitive behavior [2]. Additional emerging applications include nanosheet architectures [23], corrosion-resistant galvanic coatings, and antibacterial coatings when $Zn(OH)_2$ is combined with graphene oxide [24]. From a structural standpoint, $Zn(OH)_2$ is an amphoteric material that typically crystallizes under ambient conditions in the orthorhombic *wülfingite* phase (ε-$Zn(OH)_2$, space group $P2_12_12_1$) [25]. Meanwhile, ZnO exhibits a well-known direct bandgap of approximately 3.37 eV at room temperature [27-29], first-principles calculations suggest that pristine $Zn(OH)_2$ possesses a substantially wider intrinsic bandgap of about 5.65 eV [27]. Experimental studies on $Zn(OH)_2$-based composites, such as those incorporating graphite oxide, have reported reduced effective bandgaps in the range of ~2.88–3.60 eV, highlighting the sensitivity of its electronic structure to chemical environment and interfacial interactions [30].

Previous studies of the $ZnO/Zn(OH)_2$ system have predominantly focused on the thermal dehydration of $Zn(OH)_2$ toward ZnO, whereas the post-annealing evolution of thermally evaporated ZnO thin films during subsequent ambient cooling has received considerably less attention [26]. In the present study, ZnO thin films prepared by thermal evaporation were subjected to controlled post-deposition annealing at 400–600 °C, followed by cooling in ambient laboratory air. Particular attention was given to the emergence of hydroxide-related crystalline features after the highest-temperature treatment and their correlation with changes in surface morphology and optical response. The novelty of this work therefore lies in the characterization of the ex situ structural and optical evolution of thermally evaporated ZnO-derived films after high-temperature treatment, rather than in claiming a directly observed bulk reverse conversion of ZnO into $Zn(OH)_2$. This distinction is important because the phase detected after cooling may reflect post-annealing surface reactions, phase coexistence, or other structural changes that cannot be resolved solely by ex situ XRD, SEM, and UV–Vis measurements.

## 2. Materials and Methods

Prior to each deposition cycle, the soda–lime glass substrates were ultrasonically cleaned in ethanol for 10 min to eliminate surface contaminants, dust particles, and residual organic impurities. ZnO thin films were subsequently prepared using a vacuum thermal evaporation technique, as schematically illustrated in Fig. 1(A). High-purity ZnO powder (Sigma-Aldrich, analytical grade >99.0%).) with a total mass of 0.06 g was used as the evaporation source for each run. The deposition process was performed under a constant current of 150 A, with a source–to–substrate separation distance of approximately 7 cm, and a total deposition time of 15 min. All depositions were carried out in a high-vacuum chamber with a base pressure of ≤ $1 \times 10^{-5}$ mbar to minimize contamination and to promote uniform film growth across the substrate surface. This controlled environment ensured reproducible deposition conditions and contributed to the consistency of the obtained thin-film samples. The thickness of the as-deposited ZnO film was approximately 140 ± 10 nm, as determined using spectroscopic ellipsometry.

After the deposition process, a series of thermal annealing treatments were performed on selected as-deposited films at three different temperatures: 400 °C, 500 °C, and 600 °C. A schematic illustration of the annealing sequence is presented in Fig. 1(B). For each experiment, the sample was placed inside a quartz tube furnace at room temperature, and the heating profile was initiated by increasing the temperature at a constant ramp rate of 30 °C/min until the target temperature was reached. The annealing dwell time at the set temperature was maintained for 1 h to ensure sufficient thermal exposure for phase evolution. Upon completion of the annealing stage, the samples were rapidly removed from the furnace and allowed to cool naturally in ambient, air-conditioned laboratory conditions (~20 °C) until thermal equilibrium with the surroundings was achieved (see Fig. 1(B)). This controlled annealing procedure was designed to induce phase transformation, improve crystallinity, and alter the microstructural and surface morphological characteristics of the films.

Multiple characterization techniques were employed to systematically evaluate the influence of thermal treatment on the structural, optical, and morphological properties of the ZnO films. XRD measurements were performed in the thin-film $2\theta$ scanning mode with a grazing incidence (~2°) configuration. This approach was selected to enhance surface sensitivity and to accurately determine phase composition, crystallite orientation, and lattice characteristics of the thin films. Optical properties were examined using a UV–Vis spectrophotometer, where the absorption spectra were recorded over the relevant wavelength range to estimate the optical bandgap and to study possible changes in electronic transitions as a function of annealing temperature. The absorption coefficient was determined using the formula $\alpha = 2.303A/t$ with A being the absorbance measurement and $t$

representing the thickness of the film. The optical properties were analyzed by means of the Tauc equation $(\alpha h\nu)^n = B\,(h\nu - E)$. For this, the team chose a direct-allowed mode of $(\alpha h\nu)^2$ versus $h\nu$.

Additionally, SEM was utilized to capture high-resolution images of the film surface, allowing a detailed assessment of microstructural features, grain morphology, and surface uniformity.

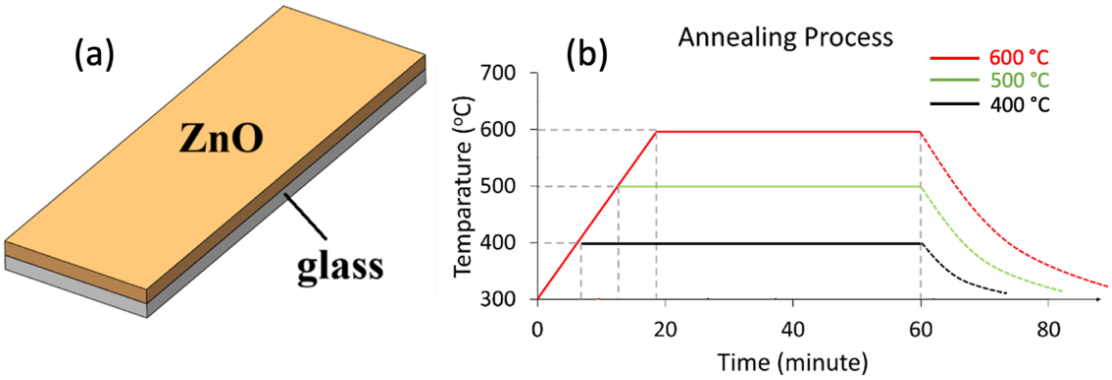



**Fig. 1:** The schematic images of (A) ZnO layer on glass substrate, and (B) the annealing process at different temperatures.

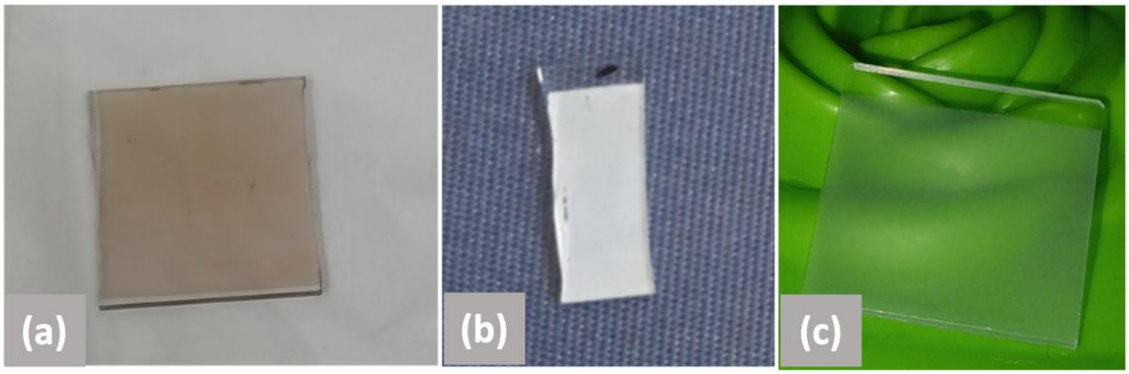



**Fig. 2:** Optical images of ZnO thin films annealed at (A) 400 °C, (B) 500 °C, and (C) 600 °C, showing a progressive enhancement in optical transparency with increasing annealing temperature. The film treated at 600 °C displays the greatest transparency.

## 3. Results and Discussion

As described in the Method section, the as-deposited ZnO films were subjected to post-annealing processes at different temperatures. Fig. 2 shows the visual appearance of the films annealed at (a) 400 °C, (b) 500 °C, and (c) 600 °C. A distinct change in optical transparency is observed as the annealing temperature increases. The film annealed at 400 °C appears brownish and relatively opaque, indicating that the microstructure may still contain a high density of structural defects or residual impurities, which act as scattering and absorption centers. When the annealing temperature is increased to 500 °C, the film exhibits a lighter coloration and reduced opacity, suggesting partial improvement in crystallinity and reduction of defect-related absorption, although the film still does not reach full optical clarity. At the highest annealing temperature of 600 °C, the ZnO thin film becomes highly transparent and visually clear. This improvement is consistent with a substantial enhancement in crystal growth, together with the possible removal of residual hydroxyl groups, adsorbed species, and defect states such as grain boundaries, oxygen vacancies, or dislocations that commonly deteriorate optical performance. The marked increase in transparency at elevated annealing temperatures highlights the importance of thermal treatment in promoting a more ordered microstructure and reducing defect density.

The crystallinity of the films was evaluated using XRD analysis. Fig. 3(A) presents the diffraction pattern of the sample annealed at 400°C. The diffractogram displays a single distinct diffraction peak located at approximately $2\theta \approx 34.4°$, which corresponds to the (002) plane of the hexagonal wurtzite ZnO structure, in agreement with the standard reference pattern (JCPDS No. 36-1451) [31]. However, the overall peak intensity is relatively weak, and the pattern is dominated by a broad amorphous halo in the $2\theta$ range of ~10°–30°, indicating that the film contains a large proportion of disordered material. In addition, a minor peak at $2\theta \approx 28.7°$ is observed and may be associated with a hydroxide-containing phase; however, the assignment remains tentative because of the weak intensity and possible overlap with other reflections. These observations suggest that the film remains largely semi-amorphous, with limited development of long-range order, and that the conversion into crystalline ZnO is incomplete under the 400 °C annealing condition.

Several additional diffraction features are observed at $2\theta \approx 12.7°$, 21.1°, 21.9°, 25.4°, 28.7°, and 33.8°. Comparison with reported reference patterns

suggests contributions from zinc hydroxide-related phases. Orthorhombic ε-$Zn(OH)_2$ (wülfingite, space group $P2_12_12_1$) has been reported according to JCPDS/PDF No. 38-0385, whereas β-$Zn(OH)_2$ has been associated with PDF No. 00-001-0360. Because several reflections may overlap with ZnO and other zinc-containing phases, the assignment of individual peaks to specific $Zn(OH)_2$ polymorphs is treated as tentative unless supported by unique reflections. Accordingly, the diffraction pattern is interpreted as evidence of a structurally heterogeneous ZnO-derived oxide–hydroxide system rather than unequivocal proof of complete conversion into a single $Zn(OH)_2$ polymorph. The estimated degree of crystallinity was approximately 39%; however, this quantity represents the relative crystalline contribution to the diffraction pattern and should not be interpreted as the quantitative phase fraction of $Zn(OH)_2$.

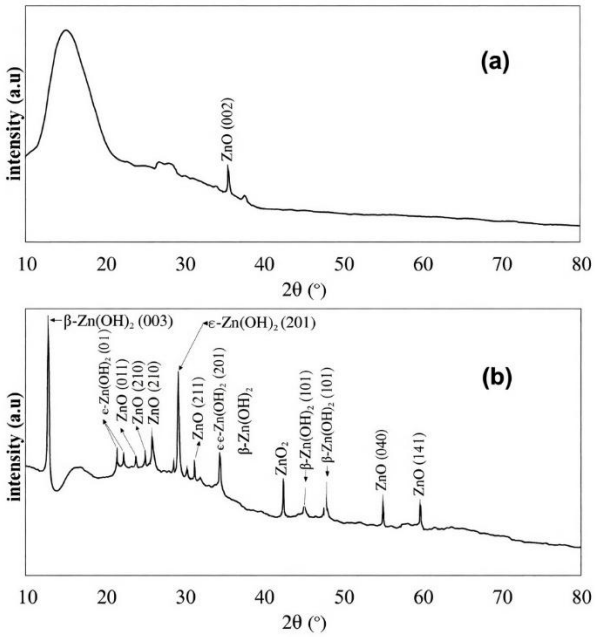



**Fig. 3:** XRD patterns of ZnO thin films annealed at (A) 400 °C and (B) 600 °C. The film annealed at 400 °C shows a dominant ZnO (002) peak characteristic of the hexagonal wurtzite structure, whereas the 600 °C sample exhibits additional peaks, indicating the presence of mixed ZnO and $Zn(OH)_2$ phases.

The formation of coexistence of $Zn(OH)_2$ and ZnO phases were also observed in the sample prepared via aqueous precipitation [35]. In contrast, the characteristic reflections of wurtzite ZnO, typically appearing at $2\theta \approx 31.7°$, 34.4°, and 36.2°, are not significantly observed in the diffractogram. Only weak features attributable to ZnO are present. A weak reflection is also observed near 47°. Because reflections from different zinc-containing phases may overlap in this region, an unambiguous assignment cannot be made solely from this peak [36, 37]. The absence of pronounced ZnO peaks, combined with the strong presence of hydroxide-related reflections, suggests that the ZnO phase did not form extensively and that the marked reduction of the characteristic ZnO reflections, together with the emergence of additional hydroxide-related reflections, indicates substantial structural evolution of the ZnO-derived film. However, the present measurements do not permit a quantitative determination of the fraction of ZnO converted into crystalline $Zn(OH)_2$.

The origin of the hydroxide-related diffraction features observed after the 600 °C treatment cannot be uniquely established from the present ex-situ measurements. In particular, the thermally induced dehydration of $Zn(OH)_2$ toward ZnO makes a direct interpretation of the observed evolution as a bulk reverse transformation of ZnO into $Zn(OH)_2$ during heating inappropriate. One possible contribution is the interaction of the ZnO-derived surface with atmospheric water during the subsequent cooling period. Such an interaction may promote surface hydroxylation; however, surface hydroxylation should be distinguished from the formation of a bulk crystalline $Zn(OH)_2$ phase. The stronger hydroxide-related diffraction features observed after the 600 °C treatment may instead reflect changes in surface morphology, defect population, surface energy, crystallographic reorganization, or chemical reactivity induced by the higher thermal budget, which could influence subsequent reactions with ambient species. The absence of comparable hydroxide-related features at 400 °C may indicate that the higher thermal treatment is required to produce the surface or microstructural state favorable for these post-annealing reactions. Nevertheless, controlled-atmosphere cooling, humidity-dependent experiments, and surface-sensitive or in situ characterization would be required to distinguish these possibilities.

The surface microstructure of the films was examined by SEM, as shown in Fig. 4. Fig. 4(A) presents the SEM micrograph of the deposited ZnO thin film, displaying a distinctly rough morphology consisting of irregularly shaped particles distributed non-uniformly across the surface. The variation in particle size indicates heterogeneous nucleation and growth during the deposition process, which is consistent with the incomplete coalescence of grains and the presence of structural defects. Additional insight is obtained from the surface topography analysis, shown in Fig. 4(B), which provides a three-dimensional representation of the surface intensity distribution derived from image processing. The color map spans from blue to red, where the red regions denote the highest intensity (corresponding to elevated surface features), while blue regions represent lower areas. The average surface intensity is 126.29, with a maximum value of 225, demonstrating significant surface height variation across the film. The calculated coefficient of variation (CV) for intensity-based roughness is 13, reflecting a moderately rough surface texture. Such a level of roughness could be associated with non-uniform crystal growth, insufficient surface diffusion during deposition, or local compositional fluctuations. The observed morphological features are expected to affect the functional performance of the ZnO films. Such surface roughness can influence photon scattering, charge transport, and adsorptive interactions, which are critical factors for applications such as gas sensors, optoelectronic

devices, and transparent conductive coatings. Therefore, understanding and controlling the growth conditions that govern surface texture is essential for optimizing the structural quality and device-relevant properties of ZnO thin films.

Fig. 4(C) shows the SEM micrograph at 5000× magnification of the film annealed at 600 °C, which, based on the XRD results, is predominantly composed of the $\beta$-$Zn(OH)_2$ phase. The surface is covered with plate-like and flower-like assemblies, which are characteristic morphologies commonly associated with zinc hydroxide systems. These hierarchical structures suggest anisotropic crystal growth, may be associated with anisotropic growth and post-annealing surface restructuring; however, the growth mechanism cannot be resolved from SEM alone. A well-defined flower-like cluster can be observed, composed of aggregated nanoscale platelets on the surface of the crystal. The formation of these micro-flowers leads to a substantial increase in effective surface area, which is highly advantageous for surface-driven applications. Fig. 4(D) displays the corresponding surface topography map, revealing an uneven spatial distribution characterized by numerous protruding peaks (represented in red) and deep valleys (gradually transitioning to blue). The measured average surface depth intensity is 119.33, with a maximum intensity of 229. The calculated coefficient of variation (CV) of 51.79 indicates significant roughness and large fluctuations in surface height across the film. Such pronounced roughness and the presence of flower-like $Zn(OH)_2$ structures can provide mechanical and chemical interaction sites, which may further improve adhesion and disruption of microbial membranes.

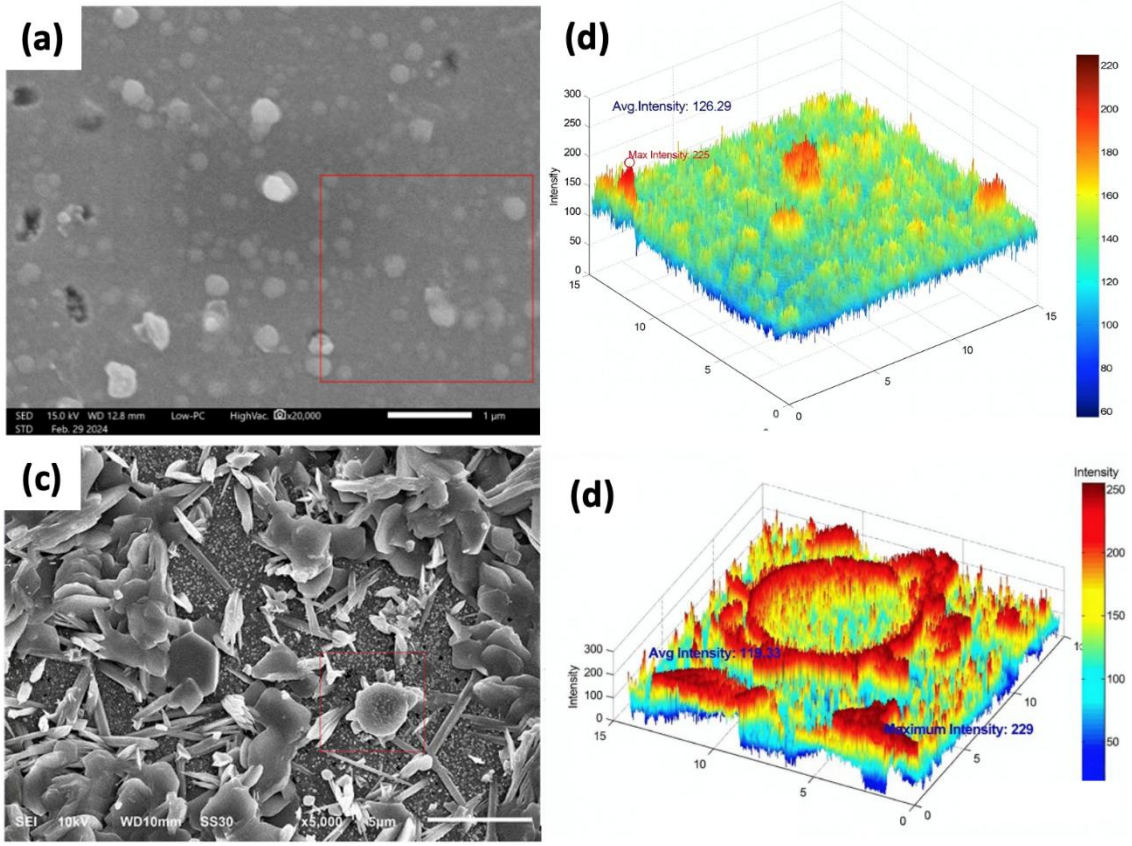



**Fig. 4:** (A) The SEM image of the as-deposited ZnO film, and (B) its corresponding surface topography, (C) that of the film annealed at 600 °C and (D) the corresponding surface topography. The as-deposited film appears to exhibit a relatively smooth and compact morphology with uniformly distributed nanoscale grains and scattered brighter agglomerated particles. While the film annealed at 600 °C exhibits a rougher surface topography, composed of densely packed plate-like and flake-like structures interspersed with elongated rod-like features and granular particles.

Nevertheless, while the morphology offers potential functional advantages, the thermal and chemical stability of $Zn(OH)_2$ must be taken into account for long-term applications. Hydroxides are generally less stable than their oxide counterparts, especially under elevated temperature or humid environments, where dehydration or structural transformation may occur. Therefore, optimizing the annealing protocol and post-treatment conditions is essential to ensure both functionality and durability of $Zn(OH)_2$-based coatings.

As explained previously, the optical properties of the films were evaluated using UV–Vis spectroscopy. Fig. 5(A) presents the absorption spectra of the ZnO-based thin films annealed at 400, 500, and 600 °C. The results show distinct absorption characteristics that evolve systematically with annealing temperature. At 400 °C, the film exhibits relatively low absorption over the measured wavelength range. This suggests that only partial improvement in crystallinity occurred, with some structural defects still present that may contribute to light scattering and non-

radiative recombination. When the annealing temperature increases to 500 °C, the absorption intensity rises, indicating further enhancement in structural order and reduced defect density. The absorption edge also becomes more defined, implying a clearer electronic transition. At 600 °C, the absorption reaches the highest level among the samples. The sharpest absorption edge is also observed at this temperature, suggesting the development of a more well-defined bandgap. The changes in absorption may originate from a combination of structural evolution, phase heterogeneity, disorder, and defect-related electronic states. Because no direct defect-sensitive measurement was performed, changes in the concentrations of oxygen vacancies or zinc interstitials cannot be quantified from UV–Vis data alone. The decrease in scattering and absorption losses at higher temperatures reflects improved structural homogeneity of the film surface, which is in agreement with the morphological observations.

Overall, these findings indicate that annealing temperature plays a key role in determining the optical response of the films. The enhanced absorption and sharper absorption edge observed at higher temperatures demonstrate improved optical quality of the $Zn(OH)_2$ thin films. This enhancement provides potential benefits in applications where efficient light interaction is required, such as in optoelectronic devices, UV-blocking coatings, and antimicrobial surfaces where light-induced activity is advantageous.

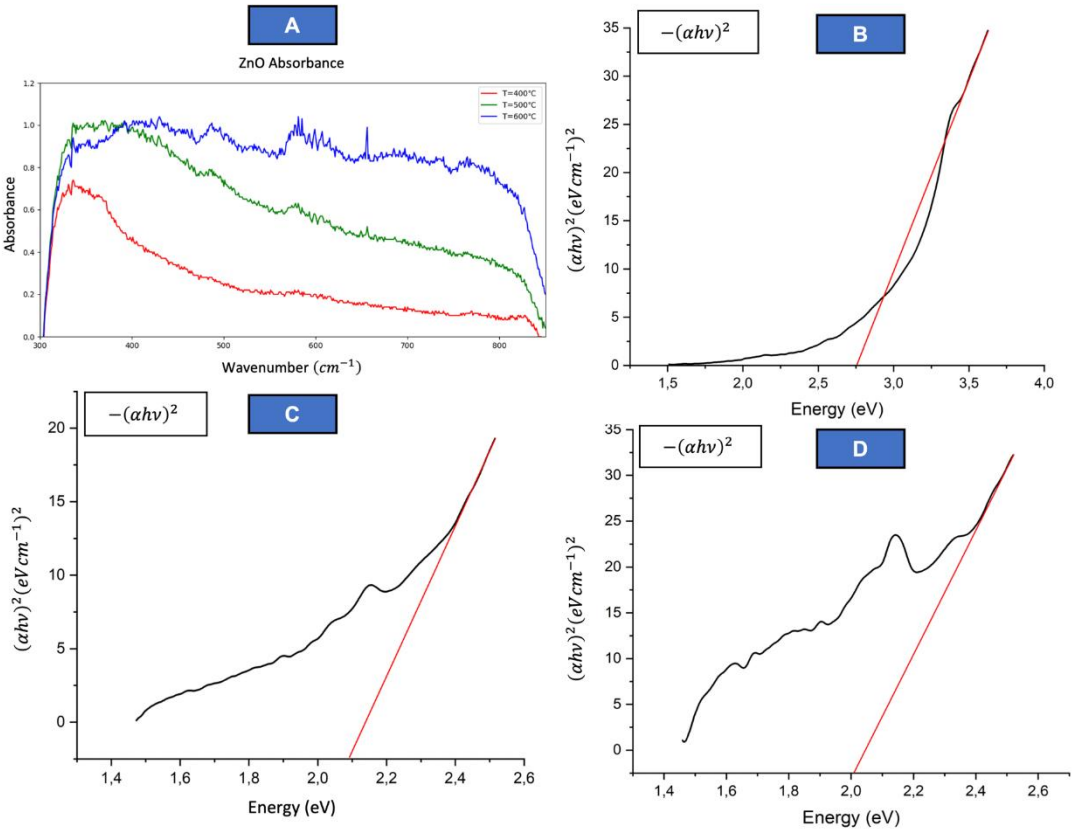



**Fig. 5:** (A) UV-Vis spectroscopy spectra of ZnO thin films annealed at different temperatures: 400 °C, 500 °C, and 600 °C, respectively. (B) Direct-allowed Tauc plots, $(\alpha hv)^2$ versus $hv$, of ZnO thin films annealed at different temperatures 400 °C, (C) 500 °C, and (D) 600 °C, respectively.

**Table 1:** The Tauc-derived optical transition energy for different annealing temperatures from 400 to 600 °C.

| Annealing Temperature | Transition model | Fitting range (eV) | $R^2$ | Apparent transition Energy |
|---|---|---|---|---|
| 400 °C | direct allowed | 3.35 – 3.55 | 0.98 | 2.75 eV |
| 500 °C | direct allowed | 2.36 – 2.50 | 0.99 | 2.10 eV |
| 600 °C | direct allowed | 2.38 – 2.50 | 0.99 | 2.00 eV |

To assess the apparent optical transition energy of the films, Tauc plot is performed to the absorption spectrum. As explained in the Materials and Method chapter, the direct-allowed transition model was selected because wurtzite ZnO is commonly treated as a direct-bandgap semiconductor. However, because the annealed films may contain mixed oxide–hydroxide phases, the resulting Tauc intercepts are interpreted as apparent optical transition energies rather than phase-specific fundamental bandgaps. Fig. 5(B)-(D) presents the Tauc plots of ZnO thin films annealed at temperatures of 400 °C, 500 °C, and 600 °C, respectively, which also experienced conversion to $Zn(OH)_2$, causing a difference in data from pure ZnO. These plots are used to determine each film's low-energy transition energy by

extrapolating the curve's linear region to the x-axis (*hν*). As the annealing temperature increases, the apparent optical transition energy values exhibit a decreasing trend. At 400 °C, the estimated Tauc-derived optical transition energy is approximately 2.75 eV. At 500 °C, it decreases to around 2.10 eV; at 600 °C, it reaches its lowest value of about 2.00 eV.

The apparent transition energies obtained from the direct-allowed Tauc representation decrease from approximately 2.75 eV at 400 °C to 2.00 eV at 600 °C. These values are substantially lower than the reported fundamental bandgaps of crystalline ZnO and pristine $Zn(OH)_2$ and therefore should not be interpreted as intrinsic phase-specific bandgaps. Instead, the low-energy intercepts may reflect sub-bandgap absorption associated with defect states, structural disorder, interfacial states, residual ZnO, or mixed oxide–hydroxide phases. The present UV–Vis measurements do not allow these contributions to be quantitatively separated.

The progressive reduction in the apparent optical transition energy with increasing annealing temperature indicates that thermal treatment significantly modifies the electronic structure of the ZnO-derived thin films. Rather than being solely attributed to improved crystallinity, this behavior is more likely associated with the combined effects of phase evolution, microstructural changes, and defect-state formation induced during annealing. As demonstrated by the XRD analysis, higher annealing temperatures promote the emergence of $Zn(OH)_2$-related phases, resulting in a mixed oxide-hydroxide system with electronic properties that differ from those of pristine ZnO.

In addition, thermal treatment can alter the concentration of intrinsic defects, such as oxygen vacancies and zinc interstitials, which introduce localized electronic states within the forbidden bandgap. These defect-related states facilitate lower-energy optical transitions and consequently reduce the apparent optical transition energy determined from the Tauc plots. Grain growth and the reduction of grain-boundary scattering during annealing may further contribute to the observed optical response by improving carrier transport and increasing optical absorption near the absorption edge.

The enhanced absorption observed at higher annealing temperatures is therefore likely the result of the combined influence of structural evolution and defect-assisted electronic transitions rather than a simple improvement in crystallinity alone. Such tunability of the optical transition energy through post-deposition annealing demonstrates that thermal processing can effectively modify the electronic and optical characteristics of ZnO-derived thin films. These findings suggest that controlled annealing provides a practical approach for tailoring the optical response of oxide–hydroxide thin-film systems for potential applications in optoelectronic devices, UV photodetectors, and photocatalytic coatings.

## 4. Conclusions

This work investigated the structural, morphological, and optical evolution of thermally evaporated ZnO thin films subjected to post-deposition annealing at 400, 500, and 600 °C. XRD revealed substantial structural changes with increasing annealing temperature. The 400 °C sample was characterized by a dominant wurtzite ZnO (002) reflection together with a broad amorphous contribution, whereas additional hydroxide-related diffraction features emerged after the 600 °C treatment. The coexistence of ZnO and hydroxide-related phases is supported by the diffraction data, although the available ex situ measurements do not permit quantitative determination of the phase fractions or definitive demonstration of complete bulk conversion of ZnO into $Zn(OH)_2$. SEM revealed pronounced morphological restructuring at 600 °C, including plate-like and flower-like surface assemblies, which are morphologically consistent with hydroxide-containing systems but are not sufficient for phase identification on their own. The Tauc-derived apparent optical transition energies decreased from approximately 2.75 eV at 400 °C to 2.10 and 2.00 eV at 500 and 600 °C, respectively. These values should not be interpreted as the intrinsic fundamental bandgaps of crystalline ZnO or $Zn(OH)_2$, but rather as low-energy optical transitions that may include contributions from defects, disorder, interfacial states, residual phases, and sub-bandgap absorption. The emergence of hydroxide-related features after high-temperature treatment may involve post-annealing interaction with ambient species during cooling, although the exact mechanism cannot be established from the present ex situ measurements. Controlled-humidity experiments and complementary surface-sensitive or in situ techniques will therefore be required to determine the origin and depth distribution of the hydroxide-related phases.


## Acknowledgement

The authors acknowledge financial support from Universitas Ahmad Dahlan: PDP S3-278/SP3/LPPM-UAD/XI/2024. I.H. Thanks to Rizki Apriyanto for helping with administration.


## References


[1] Jiang, J.; Liu, X. X.; Han, J.; Hu, K.; Chen, J. S. Self-Supported Sheets-on-Wire $CuO@Ni(OH)_2/Zn(OH)_2$ Nanoarrays for High-Performance Flexible Quasi-Solid-State Supercapacitor. *Processes* **2021**, *9*, 680. https://doi.org/10.3390/pr9040680 (MDPI)

[2] Mancharkar, A. A.; et al. Synthesis and Characterization of Zinc Hydroxide $Zn(OH)_2$ Thin Film for High-Performance Supercapacitors Using SILAR Method. *J. Mater. Sci.: Mater. Electron.* **2024**, *35*, 2019. https://doi.org/10.1007/s10854-024-13768-x.

[3] Sood, S.; et al. Enhancing Optoelectronic Performance Through Rare-Earth-Doped ZnO: Insights and Applications. *Photonics* **2025**, *12*, 454. https://doi.org/10.3390/photonics12050454

[4] Xu, X.; Cui, Q.; Jin, Y.; Guo, X. Low-Voltage Zinc Oxide Thin-Film Transistors with Solution-Processed Channel and Dielectric Layers below 150 °C. *Appl. Phys. Lett.* **2012**, *101*, 223501. https://doi.org/10.1063/1.4767048

[5] Postica, V.; et al. Tuning ZnO Sensors Reactivity toward Volatile Organic Compounds via Ag Doping and Nanoparticle Functionalization. *ACS Appl. Mater. Interfaces* **2019**, *11*, 31452–31466.https://doi.org/10.1021/acsami.9b07275

[6] Guye, M. E.; Egualle, F. K.; Appiah-Ntiamoah, R.; Kassahun, S. K.; Kim, H. Synergetic Effect of Optimized β-$Zn(OH)_2$/ZnO Heterostructure toward Electrochemical Dopamine Detection. *J. Alloys Compd.* **2024**, *1002*, 175184. https://doi.org/10.1016/j.jallcom.2024.175184

[7] Faheem, M.; Siddiqi, H. M.; Habib, A.; Shahid, M.; Afzal, A. ZnO/$Zn(OH)_2$ Nanoparticles and Self-Cleaning Coatings for the Photocatalytic Degradation of Organic Pollutants. *Front. Environ. Sci.* **2022**, *10*, 965925. https://doi.org/10.3389/fenvs.2022.965925

[8] Juang, S.-E.; Chin, N.-C.; Chang, Y.-C.; Chou, C.-M. Fabrication of $ZnCo_2O_4$–$Zn(OH)_2$ Microspheres on Carbon Cloth for Photocatalytic Decomposition of Tetracycline. *Molecules* **2024**, *29*, 4054. https://doi.org/10.3390/molecules29174054

[9] Baig, A.; Siddique, M.; Panchal, S. A Review of Visible-Light-Active Zinc Oxide Photocatalysts for Environmental Application. *Catalysts* **2025**, *15*, 100. https://doi.org/10.3390/catal15020100

[10] Diguna, L. J.; et al. Optical and Photodetection Properties of ZnO Nanoparticles Recovered from Zn Dross. *Crystals* **2020**, *11*, 6. https://doi.org/10.3390/cryst11010006

[11] Haque, S.; Faidah, H.; Ashgar, S.; Abujamel, T.; Mokhtar, J.; Almuhayawi, M. Green Synthesis of $Zn(OH)_2$/ZnO-Based Bionanocomposite Using Pomegranate Peels and Its Application in the Degradation of Bacterial Biofilm. *Nanomaterials* **2022**, *12*, 3458. https://doi.org/10.3390/nano12193458

[12] Choi, W. S.; Chisholm, M. F.; Singh, D. J.; Choi, T.; Jellison, G. E., Jr.; Lee, H. N. Wide Bandgap Tunability in Complex Transition Metal Oxides by Site-Specific Substitution. *Nat. Commun.* **2012**, *3*, 689. https://doi.org/10.1038/ncomms1690.

[13] Danish, M. S. S.; et al. A Systematic Review of Metal Oxide Applications for Energy and Environmental Sustainability. *Metals* **2020**, *10*, 1604. https://doi.org/10.3390/met10121604

[14] Batzill, M.; Diebold, U. The Surface and Materials Science of Tin Oxide. *Prog. Surf. Sci.* **2005**, *79*, 47–154. https://doi.org/10.1016/j.progsurf.2005.09.002

[15] Ohring, M. *Materials Science of Thin Films: Deposition and Structure*; Academic Press: San Diego, CA, **2002**.

[16] Raha, S.; Ahmaruzzaman, M. ZnO Nanostructured Materials and Their Potential Applications: Progress, Challenges and Perspectives. *Nanoscale Adv.* **2022**, *4*, 1868–1925. 10.1039/D1NA00880C

[17] Wisz, G.; Virt, I.; Sagan, P.; Potera, P.; Yavorskyi, R. Structural, Optical and Electrical Properties of Zinc Oxide Layers Produced by Pulsed Laser Deposition Method. *Nanoscale Res. Lett.* **2017**, *12*, 253. https://doi.org/10.1186/s11671-017-2033-9.

[18] Cruz, M. A.; Ceballos-Sanchez, O.; Luévano-Hipólito, E.; Torres-Martínez, L. ZnO Thin Films Deposited by RF Magnetron Sputtering: Effects of the Annealing and Atmosphere Conditions on the Photocatalytic Hydrogen Production. *Int. J. Hydrogen Energy* **2018**, *43*, 10301–10310. https://doi.org/10.1016/j.ijhydene.2018.04.054

[19] Suehiro, S.; Kimura, T.; Yokoe, D.; Takahashi, S. Synthesis of Highly c-Axis-Oriented ZnO Thin Films Using Novel Laser-Enhanced Electrospray CVD Under Atmospheric Pressure. *CrystEngComm* **2017**, *19*, 5995–6001. https://doi.org/10.1039/C7CE01333G

[20] Li, Y.; et al. Tuning the Surface Morphologies and Properties of ZnO Films by the Design of Interfacial Layer. *Nanoscale Res. Lett.* **2017**, *12*, 551. https://doi.org/10.1186/s11671-017-2301-8.

[21] Djurišić, A. B.; Ng, A. M. C.; Chen, X. ZnO Nanostructures for Optoelectronics: Material Properties and Device Applications. *Prog. Quantum Electron.* **2010**, *34*, 191–259. https://doi.org/10.1016/j.pquantelec.2010.04.001

[22] Karakawa, M.; Sugahara, T.; Hirose, Y.; Suganuma, K.; Aso, Y. Thin Film of Amorphous Zinc Hydroxide Semiconductor for Optical Devices with an Energy-Efficient Beneficial Coating by Metal Organic Decomposition Process. *Sci. Rep.* **2018**, *8*, 10839. https://doi.org/10.1038/s41598-018-27953-6.

[23] Altuntasoglu, O.; Matsuda, Y.; Ida, S.; Matsumoto, Y. Syntheses of Zinc Oxide and Zinc Hydroxide Single Nanosheets. *Chem. Mater.* **2010**, *22*, 3158–3164. https://doi.org/10.1021/cm100152q.

[24] Sanchez, J. A.; Materon, L.; Parsons, J. G.; Alcoutlabi, M. Synthesis, Characterization, and Antibacterial Activity of Graphene Oxide/Zinc Hydroxide Nanocomposites. *Appl. Sci.* **2024**, *14*, 6274. https://doi.org/10.3390/app14146274.

[25] Schmetzer, K.; Schnorrer-Köhler, G.; Medenbach, O. Wülfingite, ε-$Zn(OH)_2$, and Simonkolleite, $Zn_5(OH)_8Cl_2{\cdot}H_2O$, Two New Minerals from Richelsdorf, Hesse, FRG. *Neues Jahrb. Mineral. Monatsh.* **1985**, *151*, 145–154.

[26] Uekawa, N.; Iahii, S.; Kojima, T.; Kakegawa, K. Formation of Porous Spherical Aggregated Structure of ZnO Nanoparticles by Low-

Temperature Heating of $Zn(OH)_2$ in Diol Solution. *Mater. Lett.* **2007**, *61*, 1729–1734. https://doi.org/10.1016/j.matlet.2006.07.164.

[27] Wang, M.; Jiang, L.; Kim, E. J.; Hahn, S. H. Electronic Structure and Optical Properties of $Zn(OH)_2$: LDA+U Calculations and Intense Yellow Luminescence. *RSC Adv.* **2015**, *5*, 87496–87503. https://doi.org/10.1039/C5RA15959A

[28] Zhang, T.; et al. Multi-Component ZnO Alloys: Bandgap Engineering, Hetero-Structures, and Optoelectronic Devices. *Mater. Sci. Eng. R Rep.* **2022**, *147*, 100661. https://doi.org/10.1016/j.mser.2021.100661

[29] Kim, M.; Seo, J.-H.; Singisetti, U.; Ma, Z. Recent Advances in Free-Standing Single Crystalline Wide Band-Gap Semiconductors and Their Applications: GaN, SiC, ZnO, β-$Ga_2O_3$, and Diamond. *J. Mater. Chem. C* **2017**, *5*, 8338–8354. https://doi.org/10.1039/C7TC02221B

[30] Islam, S. Z.; et al. Structural and Optical Characterization of $Zn(OH)_2$ and Its Composites with Graphite Oxides. *Opt. Lett.* **2013**, *38*, 962–964. https://doi.org/10.1364/OL.38.000962

[31] He, X.; et al. Flexible Surface Acoustic Wave Based Temperature and Humidity Sensors. *MRS Online Proc. Libr.* **2014**, *1659*, 75–80. https://doi.org/10.1557/opl.2014.111.

[32] Ghica, D.; Vlaicu, I. D.; Stefan, M.; Nistor, L. C.; Nistor, S. V. On the Agent Role of $Mn^{2+}$ in Redirecting the Synthesis of $Zn(OH)_2$ toward Nano-ZnO with Variable Morphology. *RSC Adv.* **2016**, *6*, 106732–106741. 10.1039/C6RA23065B

[33] Bulla, S. S.; Bhajantri, R.; Chavan, C.; Sakthipandi, K. Synthesis and Characterization of Polythiophene/Zinc Oxide Nanocomposites for Chemiresistor Organic Vapor-Sensing Application. *J. Polym. Res.* **2021**, *28*, 251. https://doi.org/10.1007/s10965-021-02618-7.

[34] Joy, M.; Iyengar, S. J.; Chakraborty, J.; Ghosh, S. Layered Double Hydroxide Using Hydrothermal Treatment: Morphology Evolution, Intercalation, and Release Kinetics of Diclofenac Sodium. *Front. Mater. Sci.* **2017**, *11*, 395–408. https://doi.org/10.1007/s11706-017-0400-1.

[35] Top, A.; Çetinkaya, H. Zinc Oxide and Zinc Hydroxide Formation via Aqueous Precipitation: Effect of the Preparation Route and Lysozyme Addition. *Mater. Chem. Phys.* **2015**, *167*, 77–87. https://doi.org/10.1016/j.matchemphys.2015.10.013.

[36] Etape, E. P.; Foba-Tendo, J.; Ngolui, L. J.; Namondo, B. V.; Yollande, F. C.; Nguimezong, M. B. N. Structural Characterization and Magnetic Properties of Undoped and Ti-Doped ZnO Nanoparticles Prepared by Modified Oxalate Route. *J. Nanomater.* **2018**, *2018*, 9072325. https://doi.org/10.1155/2018/9072325.

[37] Bergs, C.; Brueck, L.; Rosencrantz, R.; Conrads, G.; Elling, L.; Pich, A. Biofunctionalized Zinc Peroxide ($ZnO_2$) Nanoparticles as Active Oxygen Sources and Antibacterial Agents. *RSC Adv.* **2017**, *7*, 38998–39010. 10.1039/C7RA06332F